ORIGINAL PAPER

physica status solidi b
www.pss-b.com

Synthesis of New Nitride Alloys with Mg by Plasma-Assisted Molecular Beam Epitaxy

Iulian Gherasoiu, Kin Man Yu, Huseyin Ekinci, Bo Cui, Michael Hawkridge, Vladimir Kuryatkov, Matthew Gaddy, Sergey A. Nikishin, and Wladek Walukiewicz*

A great deal of work is currently devoted to the development of new semiconductor alloys that can expand the range of material properties and device applications. Although group-III nitride alloys are attractive materials owing to the wide range of tunable direct bandgaps and other suitable properties, the material choices are limited to only a few binary and ternary alloys. This situation is due in part to the limitations of the conventional deposition methods, such as chemical vapor deposition, requiring high temperature and high pressure to synthesize a wider range of metastable alloys. In this context, the synthesis of previously unreported quaternary nitride alloys including Mg—(InGaMg)N—is presented. These alloys, with a tunable bandgap and good crystallinity, extend the group of the materials that may be suitable for the fabrication of optoelectronic devices. The method is based on the conventional plasma-assisted molecular beam epitaxy (PA-MBE), using a flux-modulation technique to enable the incorporation of all elements reaching the growth surface. In addition to detailed experimental characterization of structural and optical properties of the Mg containing nitride alloys, computations on their electronic band structures are also carried out.

1. Introduction

Direct bandgap semiconductor alloys are attractive due to their wide-ranging application for optoelectronic devices, such as light emitting diodes (LEDs), lasers, and solar cells. Moreover, among the semiconductor materials with a direct bandgap, many contain toxic elements (As, Cd, Pb, etc.), whereas for most of their alloys, the direct bandgap can be adjusted only over a narrow range. In contrast, nitride semiconductors are chemically stable and are considered benign for the environment, whereas their direct bandgap can be tailored from 6.2 eV (AlN) to 0.6 eV (InN).[1,2] This bandgap range practically covers the entire UV-visible spectrum and includes the common fiber optic wavelengths down to 1550 nm (0.79 eV).

Although the fabrication of high brightness LEDs, UV LEDs, blue lasers, and high mobility transistors (HEMTs) has been enabled by the synthesis of various nitride alloys, the field of photovoltaic devices has yet to take advantage of their favorable properties.[3] This is due to the fact that relatively thick films of InGaN or InAlN alloys required for solar cell fabrication have high density of point defects as well as dislocations, which originate at the interface with the substrate due to the heteroepitaxy process. These crystalline defects give rise to carrier recombination centers, reducing the external quantum efficiency of the solar devices built with these alloys. In addition, InGaN alloys with an indium fraction larger than 35% develop an electron accumulation layer at the surface (or interface) due to the pinning of the Fermi level above the conduction band edge.[4] The electron accumulation in these In-rich InGaN alloys will likely impede the formation of the depletion region in a P/N junction structure, thus making

Prof. I. Gherasoiu
College of Engineering
SUNY Polytechnic Institute
Utica, NY 13502, USA
E-mail: gherasi@sunypoly.edu

Prof. K. Man Yu
Department of Physics
City University of Hong Kong
83 Tat Chee Ave., Kowloon Tong, Hong Kong

Prof. K. Man Yu, Dr. W. Walukiewicz
Material Sciences Division
Lawrence Berkeley National Laboratory
Berkeley, CA 94720, USA

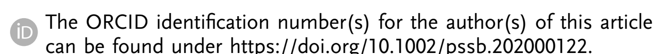
The ORCID identification number(s) for the author(s) of this article can be found under https://doi.org/10.1002/pssb.202000122.

DOI: 10.1002/pssb.202000122

Dr. H. Ekinci, Prof. B. Cui
Waterloo Institute for Nanotechnology (WIN)
University of Waterloo
200 University Ave. West, Waterloo, Ontario N2L 3G1, Canada

Dr. H. Ekinci
Department of Physics
Erzincan Binali Yıldırım University
24100 Erzincan, Turkey

Dr. M. Hawkridge
PANalytical
117 Flanders Rd., Westborough, MA 01581, USA

Dr. V. Kuryatkov, M. Gaddy, Prof. S. A. Nikishin
Nano Tech Center
Department of Electrical and Computer Engineering
Texas Tech University
2500 Broadway, Lubbock, TX 79409, USA

© 2020 WILEY-VCH Verlag GmbH & Co. KGaA, Weinheim

them unable to separate the electron–hole pairs that are excited in this region. These challenges have encouraged the search for new nitride alloys through experimental as well as computational methods.[5–13]

In this article, we report on the synthesis of novel group-III nitride alloys with Mg ($Ga_xMg_{1-x}N$ and $In_yGa_xMg_zN$). Properties of these alloys are characterized using a wide spectrum of methods, including scanning electron microscopy (SEM), cathodoluminescence (CL), energy dispersive spectroscopy (EDS), high-resolution X-ray diffraction (XRD), secondary ion mass spectroscopy (SIMS), Rutherford backscattering spectroscopy (RBS), electrochemical capacitance voltage (ECV), and high-resolution transmission electron microscopy (HRTEM). Band structures of these alloys are determined and compared with those of GaN and InGaN using the first-principle computational methods.

2. Experimental Section

The InGaN thin films were grown by plasma-assisted molecular beam epitaxy (PA-MBE) on 5 μm thick GaN-on-sapphire templates using a production style MBE system (GEN 200) equipped with two radio-frequency (RF) plasma sources and effusion cells for Al, Ga, In, Ge, and Mg. The epitaxial growth of InGaMgN was performed at a temperature of 565 °C. The beam equivalent pressure (BEP) of the Mg flux at the growth surface was varied in the range from 1×10^{-9} to 1.62×10^{-7} Torr by changing the effusion cell temperature from 300 to 390 °C. Group-III fluxes (Ga, In) were maintained constant at 1.0×10^{-7} and 5.5×10^{-7} Torr, respectively, whereas the total nitrogen flow for both plasma sources was maintained at 6.4 sccm. In a plasma system, the ion density can be indirectly assessed through the drag caused by the electrostatic forces between the ionized species. The increase in the resistance to the flow of the ions—a slowdown—through the plasma bulb produces an increase in the pressure at the gas entry point of the system. Therefore, convection-enhanced Pirani pressure gauges were installed at the gas entry point of the plasma bulb of both plasma sources to provide pressure measurements. The measurements allow for a better control of the plasma formation process providing information that can be used reliably to assess the differences between the two plasma sources and observe the changes along the operational life of each source. For the nitrogen flow specified, and plasma bulb apertures supplied with the Uni-Bulb RF plasma sources, the pressure measured by the convection gauge changes from ≈8 Torr at flow with no-plasma to ≈30 Torr when plasma stabilizes at an input power of 400 W, respectively. As the sensing element of the Pirani gauge is not in direct contact with the plasma, the changes of the pressure reading are solely due to the changes in the gas flow properties. For the conditions specified, the changes along the operation lifetime of the plasma bulb have been related to changes of the bulb conductance due to the gradual clogging of the apertures.

A thin GaN film was first grown at a temperature of 790 °C over the GaN template, followed by the opening of the indium and magnesium shutters allowing In and Mg to reach the growth surface. During the growth, the III/V ratio at the growth surface was controlled through continuous On/Off shuttering of the effusion cells as described in the literature recently.[14]

Two sets of samples were grown. For the first set (A series) while the In, Ga, and N_2 fluxes were maintained constant, the Mg flux was modified by varying the effusion cell temperature. For the second set of samples (B series), the Mg flux was controlled through the lowering of the cell temperature and through the On/Off shuttering of the Mg effusion cell with a ratio of 1/3, as shown in **Figure 1**.

3. Results and Discussion

3.1. SIMS, RBS, and RBS Channeling Analysis

After the growth, the films were characterized by SIMS and RBS (both in random and channeling orientations) to determine their structural properties and composition. The concentrations of the In, Ga, and Mg throughout the film were measured by SIMS, and the values presented in **Table 1** are the concentrations at 50 nm below the film surface.

It was found that the indium incorporation in the film was strongly suppressed when the Mg flux with values between 8×10^{-9} and 1.6×10^{-7} Torr was arriving continuously at the growth surface. For the first set of samples A (grown with continuous Mg flux), In fractions between 0.1% and 4.6% were

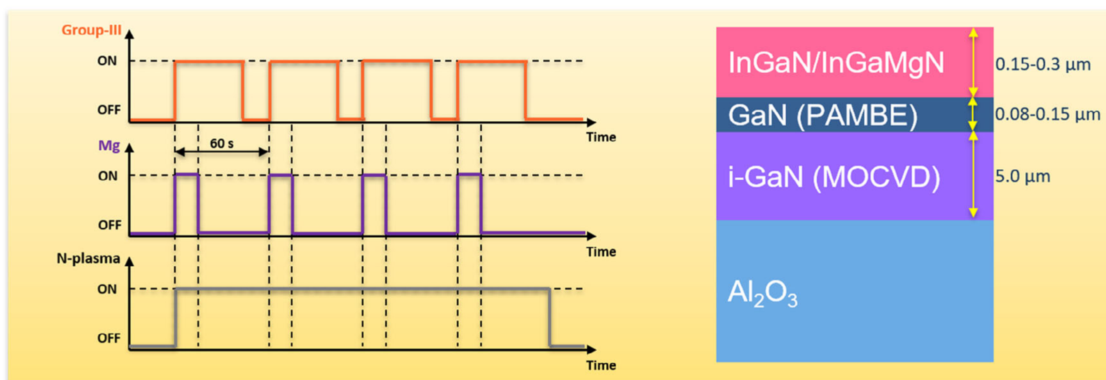

Figure 1. Modulation of the Mg flux, for the control of Mg arrival at the growth surface, sample series B. The sample structure including the InGaMgN alloys is presented at the right side of the panel.

© 2020 WILEY-VCH Verlag GmbH & Co. KGaA, Weinheim

Table 1. InGaMgN alloys obtained during the two experiments and the elemental concentrations estimated from SIMS data at a depth of 50 nm. Conduction type was determined using the ECV method. Sample group A was grown with continuous Mg flux, whereas sample group B was grown with shuttered Mg flux.

Sample ID	In [%]	Ga [%]	Mg [%]	Mg BEP [Torr]	T_{Mg} [°C]	Growth rate [nm min^{-1}]	ECV
A0	32.0	68.0	0	n.a.	n.a.	1.38	n-type
A1	0.1	90.8	9.1	1.6×10^{-7}	390	1.03	n-type
A2	0.2	90.7	9.1	1.1×10^{-7}	380	0.92	Resistive
A3	0.3	6	9.1	6.8×10^{-8}	370	1.08	Resistive
A4	4.6	88.4	7.0	7.8×10^{-9}	320	1.0	n- and p-type
B1	29.7	62.6	7.7	5.0×10^{-9}	335	1.64	n- and p-type
B2	32.5	63.9	3.6	2.7×10^{-9}	320	1.83	p-type
B3	38.7	59.7	1.6	1.1×10^{-9}	300	1.44	p-type

measured by SIMS. This strong In suppression was not observed for the B-series samples when the Mg shutter was actuated intermittently during the growth. In this way, at the surface, alternating layers of In/Ga and In/Ga/Mg will react with nitrogen radicals to form the nitride alloy, thus resulting in layers with a higher In content.

Representative SIMS elemental depth profiles of the concentrations of In, Ga, and Mg are presented in **Figure 2** for the case of continuous Mg arrival at the surface (sample A1) and for the case of periodically shuttered Mg flux (sample B1), respectively.

In the case of the growth with the intermittent Mg arrival at the surface, in contrast to the case with continuous Mg arrival, In fraction not only recovers but also increases over the level of the sample without Mg (A0 in Table 1). The increase in the In fraction together with the increase in the growth rate suggests a change in the mechanism of In incorporation that becomes more efficient and favors the incorporation of In over that of Ga. This effect has been observed and explained before through the formation of MgN radicals that prevent the recombination and formation of N_2 molecules followed by desorption.[15] **Figure 3** presents the effect of the Mg arrival mode at the growth surface on the Mg and In concentrations in the film. Indium fraction is found to have an inverse correlation to both the Mg flux BEP and the Mg concentration measured by SIMS. It is remarkable that a loss of indium takes place during the continuous arrival of Mg,

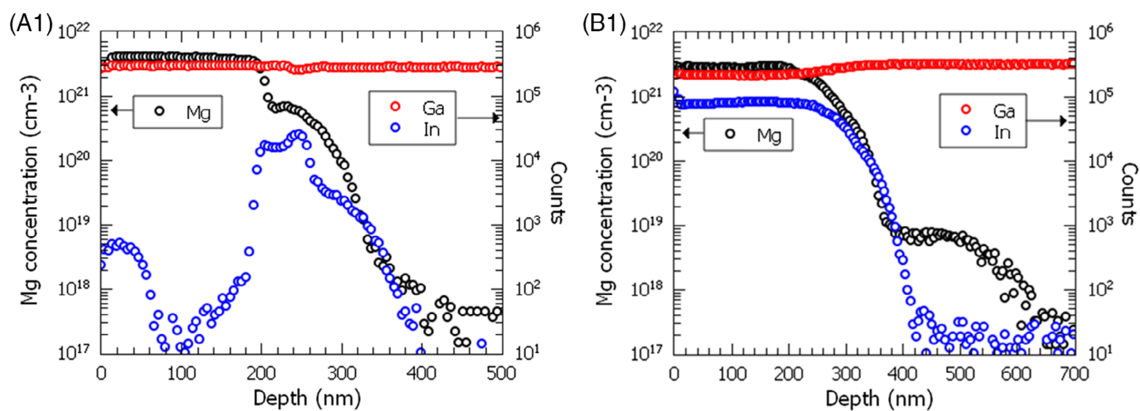

Figure 2. SIMS elemental depth profiles of samples A1 and B1.

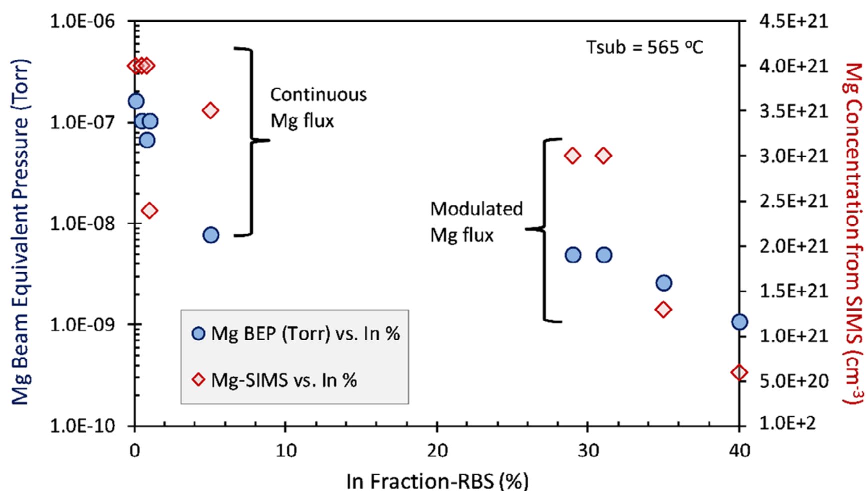

Figure 3. The effect of Mg delivery mode on the Mg and In concentrations.

© 2020 WILEY-VCH Verlag GmbH & Co. KGaA, Weinheim

whereas the intermittent arrival preserves the ability of In to incorporate.

For both methods of Mg delivery, it is noticeable that the concentration of Mg in the films is about 2–3 orders of magnitude larger than the concentrations typically required for the p-doping of the InGaN (10^{17}–10^{18} cm^{-3}). These large concentrations (2–9%) indicate the formation of quaternary alloys of InGaMgN. In group A samples, the exclusion of In from the lattice leads to the formation of In-poor InGaMgN alloys with the exception of sample A4 for which In concentration is ≈5%. Thus, samples A1–A3 can be considered as In-doped GaMgN alloys. We note that the synthesis of GaMgN alloy has been achieved previously using a high temperature (1227 °C) and high pressure (1.5 GPa) liquid phase epitaxy process.[16] Group B samples can be considered as InGaMgN alloy with Mg fractions ranging from ≈8% to ≈1.5%.

For RBS measurements, a 2 MeV $^4He^+$ beam was generated by a Van de Graff accelerator, and the scattered ions were collected at a backscattered angle of 165°. The beam was focused on the sample surface in a circular area with a diameter of ≈1 mm. The RBS data were analyzed using the RUMP software package[17] to obtain the composition and the depth profile of the various elements in the film.

Figure 4 shows the RBS spectra for samples A1 and B1 in both the random (black) and <0001> channeling direction (green) together with the RUMP best fit simulated spectra (red). In both cases, the analysis of the RBS data using the RUMP software produces the best fit when ≈8% of Mg is included in the InGaMgN layer.

RBS spectrum taken from the GaMgN sample (A1) with ≈0.1% In in the <0001> aligned direction shows much reduced scattering yields with a normalized yield χ (ratio of the channeled to random yields) of ≈0.15 at the surface and 0.21 at 400 nm below the surface. For comparison, for GaN epitaxial layers grown by MBE or metalorganic chemical vapor deposition (MOCVD), normalized yields of $\chi = 0.014$ at the surface and 0.023 at 400 nm below surface were measured. The higher χ values indicate that although the GaMgN layer is epitaxially grown on the GaN buffer layer, it has a considerable density of crystalline defects that dechanneled the ion beam. In contrast, the InGaMgN sample (B1) has normalized yield χ that is close to 1. This result can be interpreted as either: 1) InGaMgN layer is epitaxial but with a very high concentration of crystalline defects; 2) InGaMgN layer is single crystalline, but the <0001> direction is not parallel with <0001> direction of GaN substrate; or 3) InGaMgN layer is polycrystalline in nature. Comparing this to a sample without Mg but with similar In content (A0), for which the value of χ is ≈0.5, it can be concluded that the incorporation of Mg in the InGaN layer significantly degrades/changes the crystalline properties of the InGaMgN film.

3.2. Electron Microscopy Analysis

The samples were further investigated by SEM and EDS to determine the morphology of the surface as well as the distribution of the elements in relation to the surface features.

The samples grown under continuous In and Mg flux exhibit a range of morphologies from relative smooth surface (A1) to a surface populated by micrometer-sized islands and nanometer-sized columns (A4).

SEM images in **Figure 5** show that sample A1 has a relatively smooth morphology interrupted by circular regions that likely have been formed under metal droplets on the surface. Noticeably, the surface of the films is populated by fine crack lines positioned 60° apart, indicating the hexagonal symmetry of the crystalline structure of the film. It can be speculated that the cracks are the result of the stress that originate from the lattice misfit between the film's lattice and that of the GaN substrate.

The morphology changes from a relatively smooth and continuous surface (A1) to a discontinuous/columnar morphology in sample A4 can be associated with the reduction of the Mg flux reaching the surface. In the series of samples exposed to continuous Mg flux, sample A1 was exposed to the highest Mg flux, whereas sample A4 was exposed to the lowest Mg flux. Similar changes have been observed in the past and were attributed to a surfactant effect of Mg on the surface of h-GaN.[18]

The compositional analysis of the near surface layers of the samples in group A using EDS mapping shown in **Figure 6** reveals that the samples with a smooth surface, such as A1

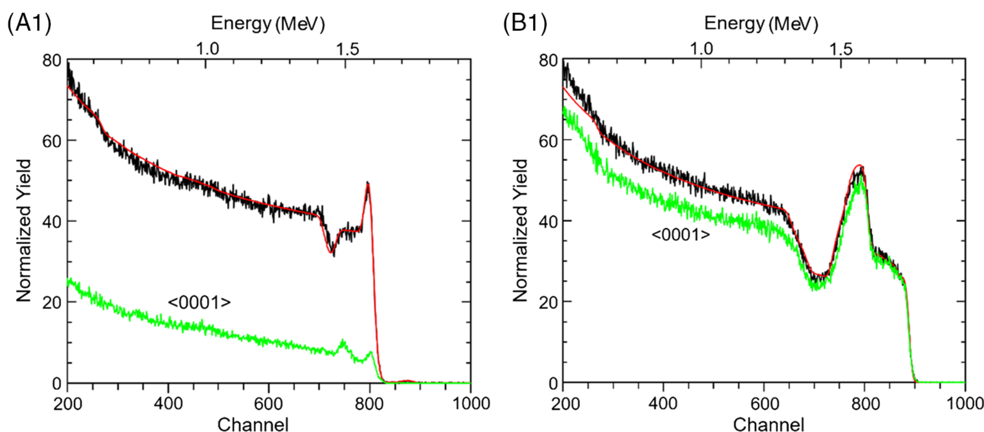

Figure 4. RBS spectra for the GaMgN (A1) and InGaMgN (B1) samples in the random (black) and <0001> aligned direction (green). Red spectra represent simulated random spectra by RUMP for the best fit layer structures of the respective cases.

© 2020 WILEY-VCH Verlag GmbH & Co. KGaA, Weinheim

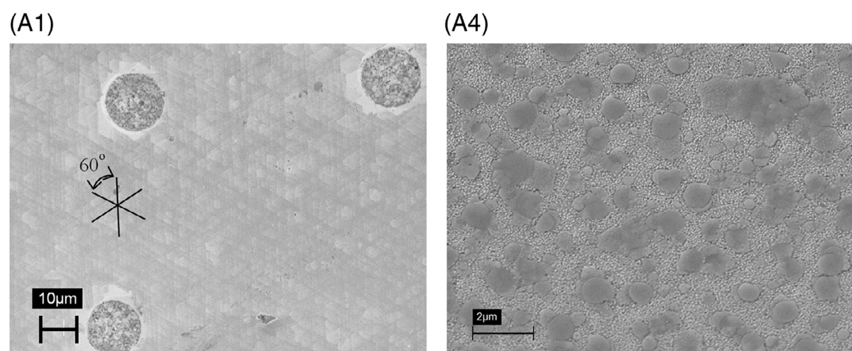

Figure 5. SEM images of the surface of samples of the InGaMgN films (A1 and A4) grown under a range of continuous Mg fluxes.

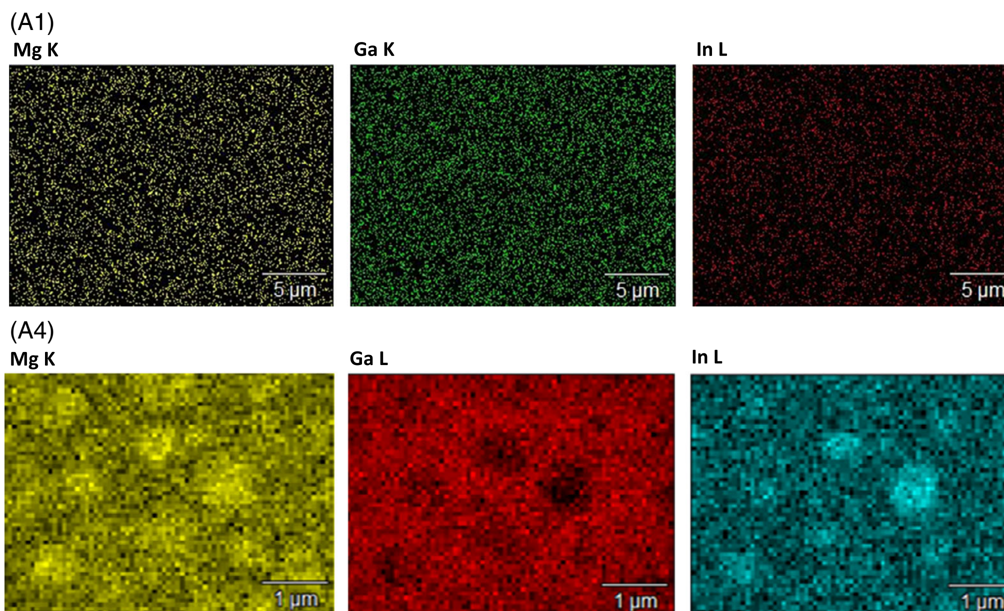

Figure 6. EDS surface maps of the surface of samples A1 and A4. From left to right, the maps presented are Mg, Ga, and In, respectively.

and A2, have a relatively uniform distribution of Mg, Ga, and In. For these samples, EDS finds Mg fractions in the range of 13.2–15.4% and group-III metal fractions of 85% Ga/1.8% In and 83% Ga/1.6% In, respectively.

In contrast, sample A4, that exhibits a discontinuous morphology, also exhibits a nonuniform elemental distribution with μm wide Mg and In-rich regions. This suggests that alloy segregation takes place during the growth. The round shape of these islands also suggests that they could have been formed under metal droplets, thus suggesting that the growth has developed under excess of group-III elements. On the other hand, the areas between the islands could have been formed under the nitrogen-rich conditions. Thus, the alloy compositional segregation could be explained by differences in the concentration of the precursors at the growth surface. Note that the average Mg, Ga, and In elemental concentrations found by EDS are somewhat different from those found by SIMS: 9.6% Mg, 87.5% Ga, and 2.9% for In. This difference may be due to the relatively higher surface sensitive nature of EDS measurement.

The samples grown under intermittent In and Mg flux have developed a morphology characterized by islands and discontinuous regions consistent with nitrogen-rich growth conditions, as shown in the SEM images of **Figure 7**. This morphology is similar to that of the samples in group A, grown under low Mg flux conditions.

EDS elemental mapping presented in **Figure 8** reveals nonuniform elemental distribution in the island-like areas. The areal maps as well as elemental concentrations measured along a linear path show that the incorporation behavior is different between the large islands and the smaller nanostructures around and similar to that exhibited by sample A4.

It can be seen that Ga fractions within the islands are lower, with an average of 49% for the island measured, when compared with the surrounding nanostructures for which the average Ga fraction is of 62.2%. In contrast, In fraction within the island is higher, with an average of 44.6%, whereas that in the surrounding nanostructures is of only 28.6%. For Mg, the average fraction measured in the material of the island is of 6.3%, whereas that in

 © 2020 WILEY-VCH Verlag GmbH & Co. KGaA, Weinheim

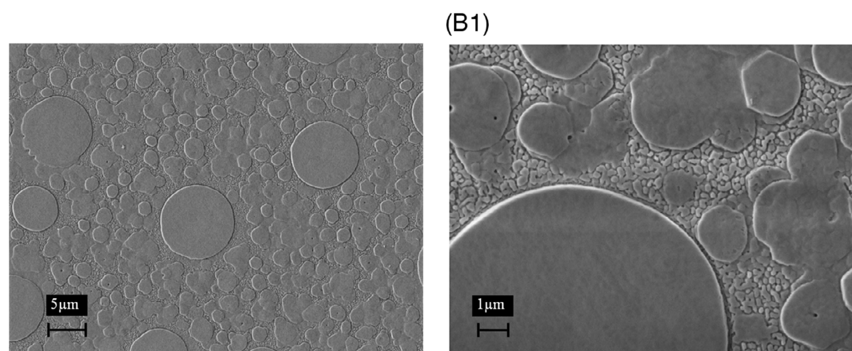

Figure 7. SEM images of the surface of the InGaMgN films (B1) grown under intermittent In and Mg flux.

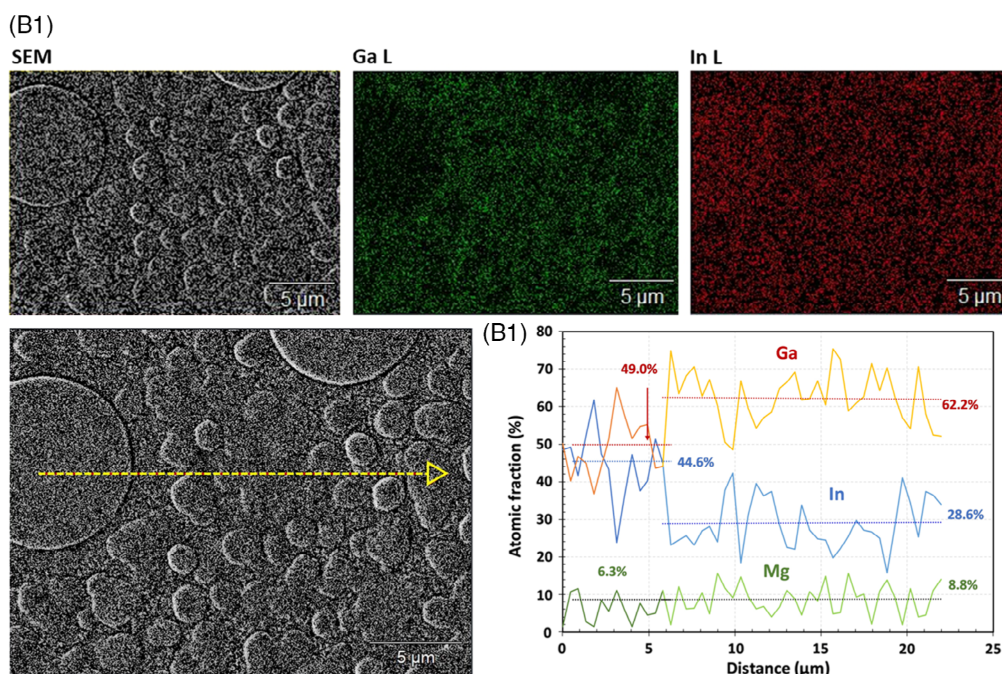

Figure 8. Top: EDS surface maps of the surface of sample B1. From left to right, the maps presented are Ga and In, respectively. Bottom: Elemental concentrations measured along the yellow path indicated in the SEM image.

the surrounding areas is ≈8.8%. The average elemental composition determined by EDS for sample B1 is 6.44% Mg, 58.7% Ga, and 34.8% In. The accuracy of the EDS determinations is related to the atomic number of the element. For elements with relatively low atomic numbers, such as Mg (12), the accuracy is within a few %, whereas for elements with higher atomic numbers, such as Ga (31) and In (49), the accuracy could be better than 1%. Accordingly, the difference between the Mg fraction within the volume of the island and outside of the island is within the accuracy of the EDS method and, therefore, is not statistically significant. Overall, the averages of the elemental fractions determined along the linear path are similar to the average composition determined through the areal mapping method.

An HRTEM image of the InGaMgN film (A2) grown under continuous In and Mg flux shown in **Figure 9** reveals that the upper layer of sample A2 exhibits a compositionally modulated structure with a period of ≈15 Å where along the *c*-direction, three unit cells of GaN are alternating with one unit cell of alloy containing Mg. This periodicity is consistent with the features observed in the diffraction pattern that exhibit a modulation length of ≈16 Å. The lack of strain and the size of the lattice spacing in the *c*-plane ($a = 3.1$ Å) suggest that the film could be a $Ga_xMg_{(1-x)}N$ hexagonal phase ($a = 3.277$ Å)[16] and not simply Mg_3N_2 ($a = 9.95$ Å).[19]

Electron energy loss spectroscopy (EELS) spectra for sample A2, shown in **Figure 10**, have been acquired to analyze the chemical composition on the cross section of the GaMgN film. In the spectrogram, Mg K-edge is located between 1305 and 1440 eV with clearly visible peaks, indicating significant Mg concentration. Ga exhibits two major edges, L_2—located at 1142 eV and L_3—located at 1115 eV. The approximate composition determined from Ga-L and Mg-K edges, after the background of the spectrum and the noise of the spectrometer were extracted, suggests a Mg content of approximately 6%,

© 2020 WILEY-VCH Verlag GmbH & Co. KGaA, Weinheim

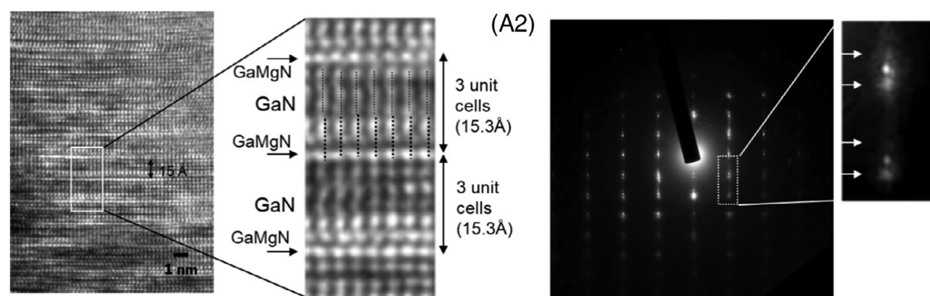

Figure 9. HRTEM image and electron diffraction pattern of the InGaMgN film (A2) grown under continuous In and Mg flux.

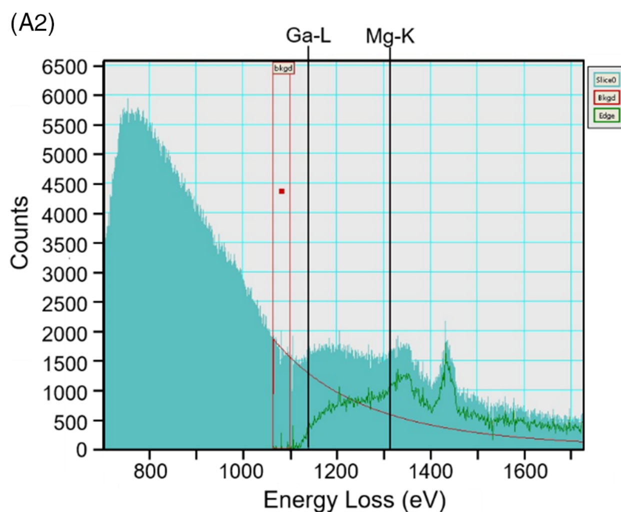

Figure 10. EELS spectra including the Ga $L_{2,3}$ edges and Mg-K edge.

which is somewhat lower than the content measured by SIMS. Nitrogen K-edge appears at around 400 eV and was not included in the graph to enhance the separation between Ga and Mg edges.

3.3. XRD Analysis

XRD measurements have been performed for all samples to identify the structure of thin films synthesized. It was assumed that these alloy films will have crystalographic planes that are parallel to GaN (0002). The diffractograms of A1 and B1 samples shown in **Figure 11** reveal diffraction peaks corresponding to the sapphire (Al_2O_3) (0006) plane and the (0002) planes of AlN, GaN, and InGaN.

Typical positions for the relaxed films of GaN and AlN (0002) are $2\theta = 34.62°$ and $2\theta = 36.03°$, respectively, whereas Al_2O_3 (0006) exhibits a peak at $2\theta = 41.8°$. Other peaks that are present in both diffractograms with $2\theta < 34°$ arise from the InGaN transition layer (a buffer between GaN and the next InGaN film) and the InGaN main layer. As only the (0002) peaks are observed, the films are either epitaxial or highly *c*-axis textured.

The diffraction peaks of sample A1 are located at 1) $2\theta = 33.88°$ and 2) $2\theta = 33.44°$. According to the lattice parameter *c*, these peaks correspond to InGaN alloys with the In concentrations of 20% and 32%, respectively. These alloys are expected to have the bandgaps of 2.61 and 2.18 eV and light emission with the wavelengths at 475 and 569 nm, respectively.

For sample B1, the two diffraction peaks are located at 1) $2\theta = 33.097°$ and 2) $2\theta = 32.57°$, corresponding to InGaN alloys with the In concentrations of 42.6% and 60%, respectively, as listed in **Table 2**. The associated bandgaps and light emission wavelengths for these InGaN alloy are of 1.84 eV (676 nm) and 1.34 eV (928 nm), respectively, and are consistent with the findings of the CL presented in the next section.

Although the EDS has found a similar average In fraction (44.6%) for the island structures, no other method, except XRD, has identified InGaN alloys with a fraction of In of 60%. Table 2 presents a summary of the XRD peaks found for these two samples.

For all the samples, the layers, including Mg, were grown at the top of the stack and SIMS, EDS, and RBS methods, all identify Mg inclusion in the crystal lattice for the uppermost layers. Using Vegard's law, we can estimate the lattice parameters of the films, assuming the composition as measured by SIMS and RBS. For sample A1, as the In fraction is low (≈0.1%), the sample can be considered as $Ga_{0.91}Mg_{0.09}N$, and the lattice constant can be interpolated from the lattice constant *c* of $Ga_{0.5}Mg_{0.5}N$ (16.065 Å) and that of GaN (5.186 Å).[20] The estimated lattice parameter along *c*-axis for sample A1 is $c = 7.14$ Å, corresponding to a (0002) diffraction peak at $2\theta = 24.9°$. The substitution of Ga with 9% of Mg atoms, in this case, produces a lattice expansion along the *c*-axis of 37.7%. However, the effect of Mg incorporation on the *c*-plane lattice constant *a* is significantly smaller. For $Ga_{0.5}Mg_{0.5}N$, the measured in-plane lattice constant is $a = 3.277$ Å, whereas the widely accepted value for GaN is $a = 3.189$ Å.[16,21] Using Vegard's law again, the *c*-plane lattice parameter for sample A1 is calculated to be $a = 3.201$ Å, an expansion of just 0.4% compared with GaN.

To estimate the lattice constant of the $In_{0.30}Ga_{0.62}Mg_{0.08}N$ (B1) alloy, we first calculate the lattice constant of $In_{0.30}Ga_{0.70}N$ as 5.337 Å using the known lattice parameters of GaN and InN. Similar to the previous case, an amount of ≈8% Ga atoms are replaced by Mg, and it is assumed that this replacement will produce a similar lattice expansion along the *c*-axis. Thus, the c-lattice constant of $In_{0.30}Ga_{0.62}Mg_{0.08}N$ is estimated to be 7.35 Å, and the corresponding (0002) diffraction peak should be located at $2\theta = 24.2°$. Similarly, the *c*-plane lattice constant of $In_{0.30}Ga_{0.70}N$ is estimated to be $a = 3.297$ Å. Assuming that the incorporation of 8% of Mg will produce an expansion of 0.4%, the expected *c*-plane lattice constant of $In_{0.30}Ga_{0.62}Mg_{0.08}N$

© 2020 WILEY-VCH Verlag GmbH & Co. KGaA, Weinheim

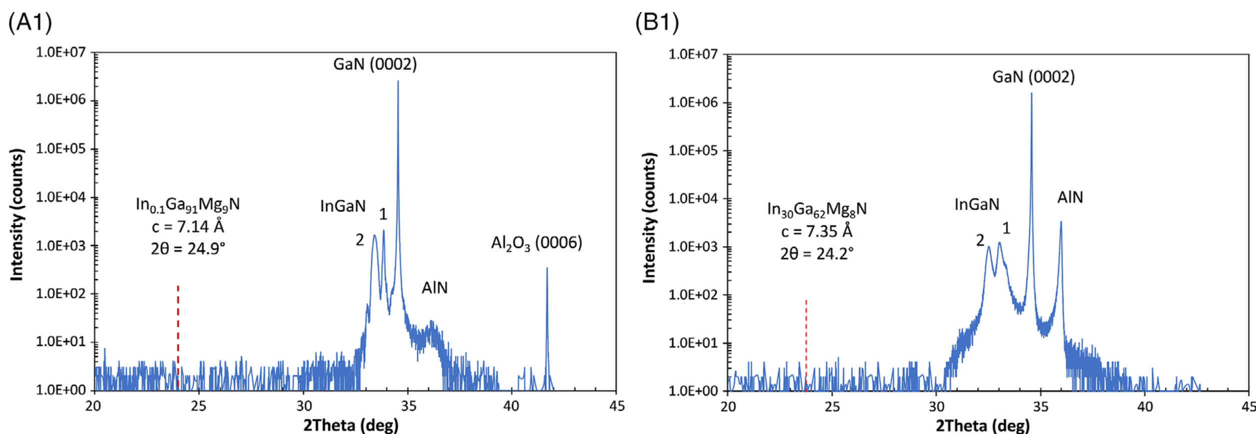

Figure 11. X-ray difractograms of the InGaMgN films A1 and B1.

Table 2. Summary of the XRD peaks of samples A1 and B1.

Sample		Al_2O_3	AlN	GaN	InGaN 1	InGaN 2
A1	XRD-2θ (deg)	41.8	36.39	34.54	33.87	33.4
	In fraction [%]	–	–	–	19.8	33.7
B1	XRD-2θ (deg)	n.a.	36.00	34.57	33.09	32.53
	In fraction [%]	–	–	–	42.6	60.4

alloy is $a = 3.309$ Å. However, no diffraction peak at either $2\theta = 24.9°$ or $24.2°$ is observable in XRD patterns shown in Figure 10. The absence of the diffraction peaks is plausible in those cases for which the *c*-axis of the crystal is not parallel with the diffraction vector and could suggest that the *c*-axis of the nitride alloys with Mg may not be parallel with that of GaN/InGaN alloys. It is, thus, obvious that a thorough XRD investigation is necessary to explore the crystallographic characteristics of the new alloys.

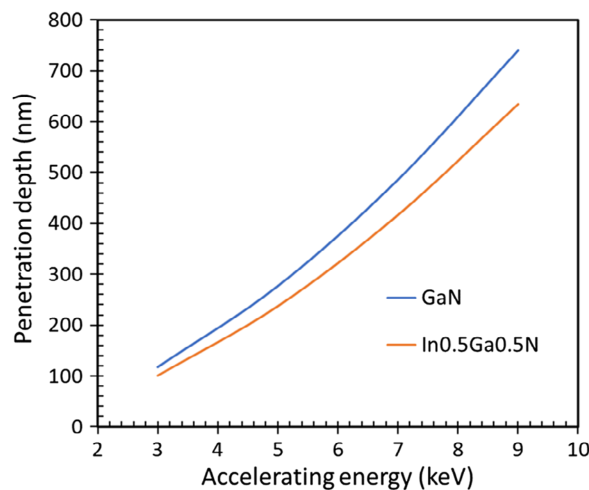

Figure 12. Penetration depth for GaN and $In_{0.5}Ga_{0.5}N$ of the electron beam as a function of accelerating energy.

3.4. Cathodoluminescence Analysis

The CL technique allows the probing of the optoelectronic properties of the material under analysis as a function of depth. A series of acceleration voltages: 3, 5, 7, and 9 kV were used to carry out the CL characterization in this work. The penetration range of the electrons depicted in **Figure 12** is estimated using the relationship suggested by Kanaya and Okayama, where the effective atomic number was calculated according to the relationship suggested by Murty.[22,23] Consequently, at a low electron energy of 3 keV, the luminescence spectra will represent the material down to a depth of ≈100 nm, whereas at a high energy of 9 keV, the spectra will represent the entire material composition down to a depth of ≈700 nm.

Figure 13 shows the CL spectra from the alloy thin films A1 and B1. Both samples A1 and B1 exhibit luminescence peaks originating from the GaN buffer layer at 3.36 and 3.4 eV. The luminescence of the relaxed GaN/sapphire at room temperature is expected at an energy of 3.43 eV (361 nm).[24] Residual stress of a semiconductor film will change its bandgap, causing a decrease when the stress is tensile or an increase in the bandgap under compressive stress. Thus, the luminescence peak of GaN buffer of sample A1 is slightly red shifted (3.36 eV) compared with the relaxed value and suggests that the GaN film is under tensile stress. Noticeably, the spectrum of sample A1 differs markedly from the CL spectrum of Mg-doped GaN for which the main feature is the donor–acceptor pair (DAP) emission at 3.28 eV.[25] In contrast, the CL spectrum of sample B1 exhibits a much narrower and less intense luminescence peak at 3.40 eV.

At lower energies, sample A1 exhibits a broad luminescence peak centered around 2.25 eV (552 nm). This broad peak extending roughly from 2.76 eV (450 nm) down to 1.91 eV (650 nm) arise from the contribution of several luminescence peaks among which InGaN with the In fractions of 20% and 34%, as determined by XRD, would be responsible for the luminescence peaks centered at 2.6 eV (475 nm) and 2.12 eV (585 nm), respectively. However, other luminescence mechanisms such as compositional segregation, local strain-induced bandgap modulation, and point defects in the film should be playing a role to account for the width and the features of the luminescence.

 © 2020 WILEY-VCH Verlag GmbH & Co. KGaA, Weinheim

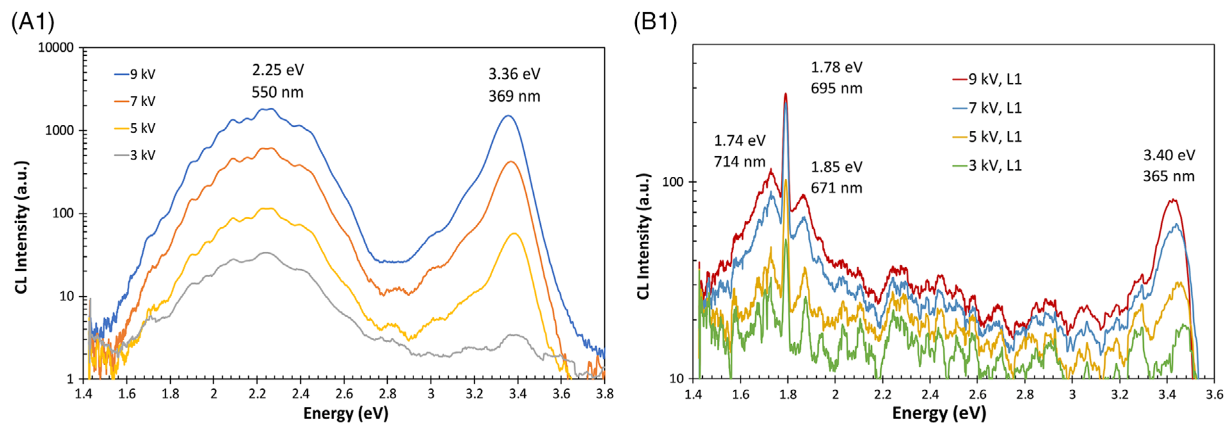

Figure 13. CL response of the InGaMgN films A1 and B1.

The first-principles calculations have shown that substitutional Mg on Ga sites (Mg_{Ga}) and nitrogen vacancies (V_N) that form a complex defect Mg_{Ga}–V_N can produce a broad emission peak centered around ≈1.8 eV in Mg-doped GaN.[26] Similarly, it was found that electrons excited to the conduction band minimum (CBM) can recombine with isolated nitrogen vacancies V_N^{3+}, producing a broad luminescence peak centered at 2.18 eV.[26] Ga vacancies, V_{Ga}, were also found to produce emission peaks at 1.72, 2.17, and 2.21 eV.[27] The CL spectrum produced in the topmost layer of sample A1 remains the dominant feature at every acceleration voltage in spite of the increase in the depth of penetration and a tenfold increase in the intensity. This suggests that the wide luminescence peak centered at 2.25 eV, although including contributions from the InGaN band-to-band luminescence at 2.6 and 2.12 eV, is dominated by the emissions originating from the recombination of excited electrons with a significant number of nitrogen (V_N^{3+}) and gallium (V_{Ga}) vacancies present in the upper layers of the sample.

The CL spectrum of sample B1 exhibits an intense and narrow luminescence peak at 1.78 eV (695 nm) that is overlapping with lower intensity luminescence peaks at 1.85 eV (671 nm) and 1.74 eV (714 nm). The most intense luminescence peak at 1.78 eV is present at all accelerations, and its origin may be ascribed to the electron transitions between the Mg_{Ga}–V_N complexes. The origin of the satellite peak with higher energy at 1.85 eV can be ascribed to the InGaN alloy with the In fraction of 42.6% determined through the XRD, whereas the peak with 1.74 eV may also originate from transitions involving gallium vacancies V_{Ga}. Finally, the InGaN alloy with an In fraction of 60.4% present in the X-ray diffractogram would generate luminescence with a wavelength of 1.34 eV (928 nm) that is outside the maximum range of detection of the CL apparatus, 1.46 eV (850 nm).

Table 3 presents a summary of the main luminescence peaks of samples A1 and B1.

Table 3. Summary of the CL peaks of samples A1 and B1.

Sample		Peak 1 GaN	Peak 2	Peak 3	Peak 4
A1	CL λ [nm]	369	475	550	585
	E_g [eV]	3.36	2.6	2.25	2.12
	In fraction [%]	–	20.1	30.1	33.5
B1	CL λ [nm]	365	671	695	714
	E_g [eV]	3.40	1.85	1.78	1.74
	In fraction [%]	–	42.6	Mg_{Ga}–V_N	46

3.5. Electronic Band Structure Calculations

Our experimental results reveal the presence of Mg containing ternary and quaternary nitride alloys in the top layers of the films grown by both the continuous and intermittent Mg flux methods. Here, we also perform modeling of material structure at the atomic level and calculate the electronic properties to better understand our experimental results. For this purpose, QuantumATK software was used. The substitution of Mg onto the group-III lattice site bears some resemblance to the case of dilute nitride alloys in which isoelectronic impurities with substantially different size and electronegativity are substituted onto the group-V lattice sites. However, Mg is not an isoelectronic impurity, with a size that is just ≈19% larger than that of Ga and an electronegativity (1.31) that is somewhat smaller than that of Ga (1.81). In the context of InGaN bonding, substitutional Mg replaces the three valence electrons of the Ga with only two electrons occupying lower energies on a 3s orbital. When used as a dopant with a fraction of less than 1%, the Mg impurity was found to induce acceptor levels above the GaN valence band edge, in the range from 124 to 212 meV, depending on Mg concentration.[28,29] For InGaN alloys, the introduction of Mg was found to induce an acceptor level above the valence band edge that depends on the In fraction, and ranging from 145 to 43 meV with increasing In content.[30,31] Thus, the presence of Mg in larger concentrations could be expected to alter the valence band structure more significantly and, at the same time, to alter the lattice spacing and symmetry.

Two types of materials were synthesized and modeled. Samples A1–A3 exhibit films of $Ga_{0.91}Mg_{0.09}N$ with less than 1% In. Therefore, for this group of samples, In is disregarded, and only GaMgN alloy is modeled. Sample B exhibits films of $In_xGa_yMg_zN$ where Mg ranges from ≈8% to ≈1.5% and the

© 2020 WILEY-VCH Verlag GmbH & Co. KGaA, Weinheim

In fraction ranges from ≈30% to ≈39%. For this work, only the quaternary alloy containing 8% Mg and 30% In was modeled.

GaMgN is assumed to have a wurtzite lattice, and the lattice parameters of the Mg-based alloys were determined by interpolating the values of the relaxed GaN lattice parameters and those of $Ga_{0.50}Mg_{0.50}N$ lattice parameters.[16,20,21] For the quaternary $In_{0.30}Ga_{0.62}Mg_{0.08}N$, the approximation of the lattice parameters was based on the structure of $In_{0.30}Ga_{0.70}N$ for which Mg was substituted to Ga and it was considered that Mg introduces a lattice dilation, proportional to the Mg concentration, as explained previously. The atomic structures were built as random alloys where Mg has been substituted randomly for Ga atoms. The GaMgN (3 × 3 × 3) supercell (SC) consists of 108 atoms of which 54 are N atoms, 49 are Ga atoms, and 5 are Mg atoms that were substituted randomly for Ga, **Figure 14**a. A similar SC of 108 atoms was used for the InGaMgN alloy, Figure 14b, and contains 54 N atoms, 35 Ga atoms, 16 In atoms, and 3 Mg atoms that were substituted on Ga sites.

In QuantumATK, the band structure of the ideal periodic crystalline material is calculated within the formalism of density functional theory (DFT) using the linear combination of atomic orbitals (LCAO), whereas the many-body electronic structure of the system is described in terms of the one-electron Kohn–Sham Hamiltonian.[32] However, the DFT implementation using Kohn–Sham approximation (KS-DFT) of the electron kinetic energy in terms of orbitals with the gradient-corrected exchange-correlation potentials (GGA) is infamous for severely underestimating the bandgaps of the semiconducting materials.[33]

Progress has been made in improving density-based approximations, through the use of meta-GGA functionals that, besides the description of electron density and its gradient, add a description of the *kinetic energy density*. This approach was shown to produce accurate bandgaps for a broad range of semiconductor materials.[34] QuantumATK allows the use of TB09 meta-GGA approximation of the exchange correlation energy to provide a more accurate description of the semiconductor bands.

The modeling of disordered solids presents significant practical interest and has been studied intensively. Effective ab initio methods developed for ideal periodic crystalline materials that rely on the translational symmetry of the repeated structure to make calculations tractable cannot be applied directly for random alloys. Random substitutional alloys lack formal translational symmetry and, thus, cannot be described by the usual representation of band-structure dispersion E(k). Instead, a SC realization is used to allow for the inclusion of the randomness of the atomic constituents. Bloch spectral functions—distribution of single-particle electronic states in energy and momentum space—are derived for all wave vectors k_i over which the effective band structure (EBS) is constructed. For a random realization, EBS is constructed by calculating a subset of averaged representative spectral functions {A(k_i,E)}. Reliable modeling that could avoid the introduction of the artifacts should be based on the use of larger size SC or by repeating the procedure for multiple random realizations and averaging all the spectral functions into the alloy EBS. This approach in which Bloch spectral functions

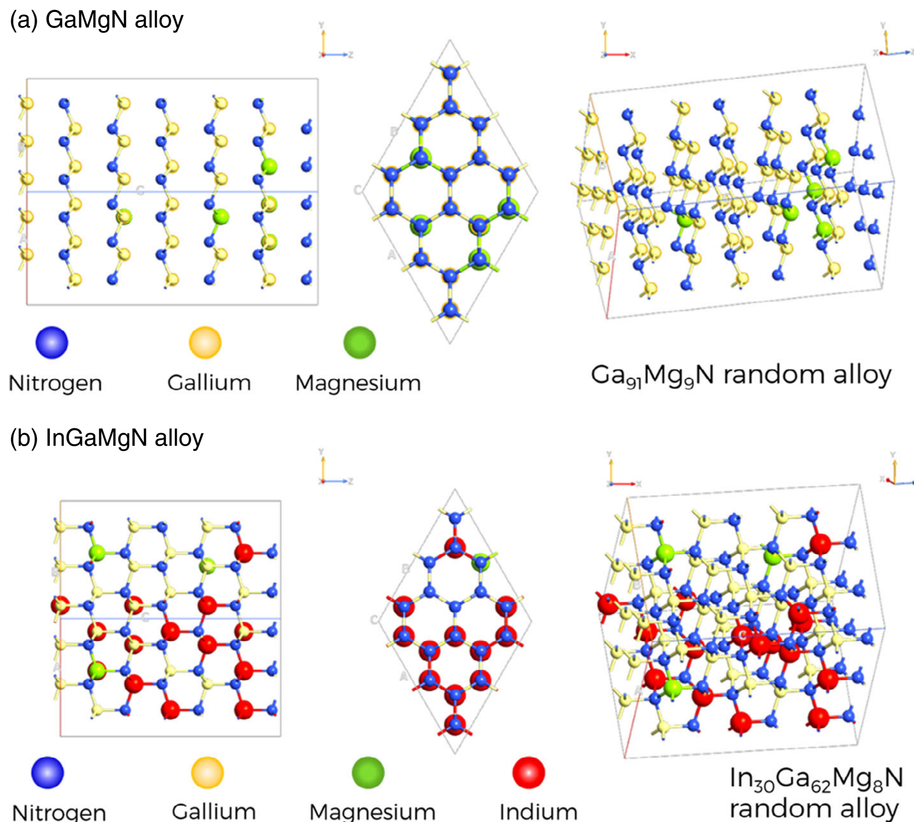

Figure 14. The (3 × 3 × 3) SCs used for the calculation of the EBSs. a) GaMgN alloy and b) InGaMgN alloy.

© 2020 WILEY-VCH Verlag GmbH & Co. KGaA, Weinheim

substitute for energy bands was introduced by Popescu and Zunger[35] and is enabled by QuantumATK software.[36,37]

EBS reveals the extent to which band characteristics are preserved or lost (shifts and broadening of the electron states) at different compositions, band indices, and k points. EBS is also important, because it was demonstrated to reproduce closely the angle-resolved photoemission measurements (ARPES).[38]

Typical electronic band structures for GaN were first modeled for the primitive $(1 \times 1 \times 1)$ unit cell and for a $(3 \times 3 \times 3)$ SC in the Brillouin zone (BZ) using KS-DFT and TB09 meta-GGA approximation and are presented in **Figure 15**a,b. The direct bandgap is noticeable at the gamma (Γ) point and has a value of $E_g = 3.44$ eV for the primitive cell and $E_g = 3.43$ eV for the SC, respectively. Both values are very close to the range of experimental values measured, at room temperature $E_g = 3.39$ eV.[39,40] The method for EBS determination was then used using a $(3 \times 3 \times 3)$ GaN SC, Figure 15c, and the results were compared. The plot of the EBS for GaN, presented in Figure 14c, exhibits a high degree of similarity with the regular GaN band layout around the high-symmetry k-points. The bandgap value obtained with the EBS is $E_g = 3.47$ eV, attesting for the effectiveness of the EBS determination method. In the case of the $Ga_{0.91}Mg_{0.09}N$ random alloy, the EBS depiction is presented in Figure 15d.

The effect of the lattice disorder translates into band splitting and broadening. The CBM remains relatively sharp at the gamma (Γ) point, whereas the valence band is split in multiple levels, akin to an impurity band related to the high concentration of Mg. The CBM and valence band maximum are located at the Γ point indicating the direct bandgap property of the $Ga_{0.91}Mg_{0.09}N$ alloy, and the gap has a value of only $E_g = 0.1$ eV. The color of the bands and the side bar represent the Bloch spectral weight. Bloch spectral weight quantifies the probability that a set of primitive cell states $|k_i n\rangle$ contribute to the SC state $|Km\rangle$ at the same energy $E_n = E_m$. For a periodic system, such as that for which the primitive cell is selected, the spectral weight can be either 1 or 0. For the disordered SC, the spectral weight can take any value between 0 and 1.

EBS was calculated in the BZ for both $In_{0.30}Ga_{0.70}N$ and $In_{0.30}Ga_{0.62}Mg_{0.08}N$ alloys, as presented in **Figure 16**. $In_{0.30}Ga_{0.70}N$ EBS shown in Figure 15a is an example of a perturbed alloy that exhibits sharp bands with a large spectral weight only around the Γ point. Elsewhere in the BZ, the disorder introduced by the presence of In is noticeable in the splitting and broadening of the bands, whereas the spectral weight is diminished. Using the equation describing the bandgap value as a function of In fraction for In(%) = 30% and a bowing coefficient $b = 1.43$, the bandgap value calculated is $E_g = 2.29$ eV.[40] The value that is determined for the $In_{0.30}Ga_{0.70}N$ alloy through the EBS method exhibits a bandgap value of $E_g = 2.33$ eV, slightly larger than the value calculated through interpolation. The Fermi energy is situated in the bandgap, as expected.

Similar to the previous alloys, the inclusion of Mg up to the concentrations analyzed (8%) does not change the direct bandgap property of the alloys. A bandgap of $E_g = 0.20$ eV that is significantly smaller than the bandgap of $In_{0.30}Ga_{0.70}N$ is determined for the $In_{0.30}Ga_{0.62}Mg_{0.08}N$ alloy.

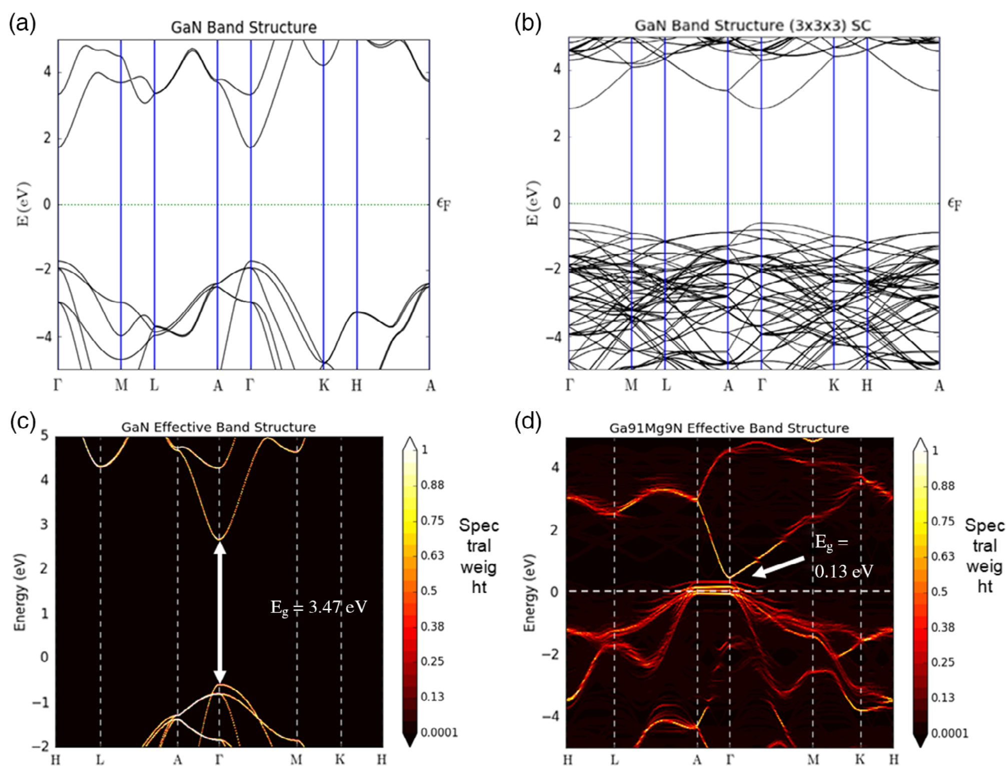

Figure 15. Electronic band structure of a) GaN primitive cell, b) GaN $(3 \times 3 \times 3)$ supercell, c) EBSs of GaN, and d) EBS of $Ga_{91}Mg_9N$ calculated in the BZ through the unfolding procedure. The Fermi energy is set to zero.

© 2020 WILEY-VCH Verlag GmbH & Co. KGaA, Weinheim

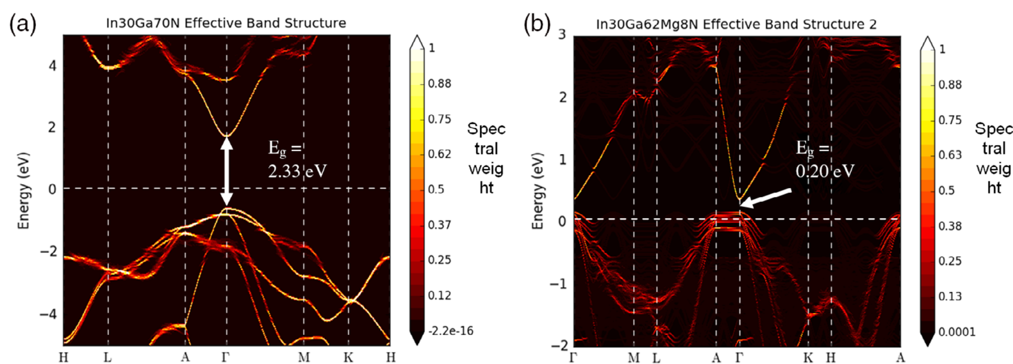

Figure 16. EBSs of a) $In_{30}Ga_{70}N$ and b) $In_{30}Ga_{62}Mg_8N$ calculated in the BZ through the unfolding procedure. The Fermi energy is set to zero.

The electronic properties of the SC are strongly perturbed when Mg is introduced in the lattice. The perturbation is the strongest in the valence band where multiple states introduced result in the lack of coherence throughout the entire BZ, whereas the spectral weights are strongly diminished. In contrast, the conduction band remains almost unperturbed at the Γ point.

In the case of the both alloys, GaMgN and InGaMgN, the calculations show two essential characteristics: 1) the addition of a fraction of Mg of 8–9% results in a drastic reduction of the bandgap from 3.39 and 2.33 eV to 0.13 and 0.2 eV, respectively, and 2) most noticeably, the Fermi level for both Mg alloys sits at the top of the valence band, suggesting that they are p-type semiconductors. The determination of such narrow bandgaps, however, was not possible using the measurement of CL transitions, as the detection limits of the CL apparatus were in the range from 6.2 eV (200 nm) to 1.46 eV (850 nm). The doping of the films was measured using the ECV method. The discontinuous nature of the films and the compositional variability of both Mg and In at the microscale makes it challenging to arrive at unambiguous conclusions regarding the dominant carriers at the surface. The results show that only two films in group B exhibit p-type conduction. The rest of the films exhibit either n-type conduction, n- and p-type conduction, or are too resistive to allow a reliable measurement.

4. Conclusion

In summary, the ability of PA-MBE to synthesize GaMgN and InGaMgN alloys with Mg fractions in the range from ≈1.5% to ≈8% is reported. In the past, only the synthesis at high-temperature and high-pressure CVD of GaMgN was reported. Characterizations of the alloy compositions using SIMS, RBS, EDS, and HRTEM all demonstrate the presence of these alloys in the topmost layers of films synthetized. Micro-characterization using EDS shows that the film composition is not uniform at the micrometer scale and depends on the growth mechanism that was dominant in each region. XRD measurements identify diffraction peaks that correspond to GaN and InGaN crystalline phases but fail to identify any diffraction originating from GaMgN and InGaMgN alloys, and hence, further investigation on the crystallographic properties of these Mg containing phases is required. CL measurements suggest phase segregation in the InGaN layers. Complex defects involving N vacancies and substitutional Mg_{Ga} may be present and produce characteristic luminescence at 1.78 eV. We plan to carry out low temperature photoluminescence measurements of this sample to better understand the origin of this spectrum feature. The first-principle modeling of the atomic structures and the calculation of the band structures using DFT and meta-GGA approximation suggest that the alloys of GaN and InGaN with Mg remain direct bandgap semiconductors, within the experimental boundaries (Mg fraction of up to 9%), with conduction enabled by hole carriers in the valence band. The limitations of detection range of the CL apparatus prevent the measurements of optical transitions with energies lower than 1.45 eV. Therefore, the existence of low CL energy emission (0.1–0.2 eV) originating from the Mg containing alloys, consistent with the results of the computation, could not be verified.

The modeling also suggests that a relatively small change of the Mg fraction in these wurtzite alloys results in a significant change of the bandgap and further that GaMgN alloys may be used as p-type semiconductor films together with n-type GaN or InGaN films to engineer new optoelectronic devices for a large range of wavelengths.

Acknowledgements

This work was supported by RoseStreet Energy Laboratory, Contract LB07003462 and US DOD/DARPA under contract W91CRB-11-C-0012. The authors also acknowledge the financial support by City U SGP, Grant No. 9380076. M.G. acknowledges the partial support from a grant #P200A 180068, from the US Department Education in the program of Graduate Assistance in the National Need (GAANN). Data analysis and visualization were aided by SciDAVis application for Scientific Data Analysis and Visualization and by Daniel's XL Toolbox add-in for Excel.

Conflict of Interest

The authors declare no conflict of interest.

Keywords

(InGaMg)N, band modeling, nitride alloys, plasma-assisted molecular beam epitaxy

© 2020 WILEY-VCH Verlag GmbH & Co. KGaA, Weinheim

Received: March 2, 2020
Revised: May 14, 2020
Published online: June 8, 2020

[1] J. Wu, W. Walukiewicz, K. M. Yu, J. W. Ager III, E. E. Haller, H. Lu, W. J. Schaff, *Appl. Phys. Lett.* **2002**, *80*, 3967.
[2] V. Yu. Davydov, A. A. Klochikhin, V. V. Emtsev, D. A. Kurdyukov, S. V. Ivanov, V. A. Vekshin, F. Bechstedt, J. Furthmüller, J. Aderhold, J. Graul, A. V. Mudryi, H. Harima, A. Hashimoto, A. Yamamoto, E. E. Haller, *Phys. Status Solidi B* **2002**, *234*, 787.
[3] S. Nakamura, T. Mukai, M. Senoh, *Appl. Phys. Lett.* **1994**, *64*, 1687.
[4] S. X. Li, K. M. Yu, J. Wu, R. E. Jones, W. Walukiewicz, J. W. Ager III, W. Shan, E. E. Haller, H. Lu, W. J. Schaff, *Phys. Rev. B* **2005**, *71*, 161201(R).
[5] A. Zerr, G. Miehe, R. Riedel, *Nat. Mater.* **2003**, *2*, 185.
[6] L. Lahourcade, N. C. Coronel, K. T. Delaney, S. K. Shukla, N. A. Spaldin, H. A. Atwater, *Adv. Mater.* **2013**, *25*, 2562.
[7] A. Zakutayev, A. J. Allen, X. Zhang, J. Vidal, Z. Cui, S. Lany, M. Yang, F. J. DiSalvo, D. S. Ginley, *Chem. Mater.* **2014**, *26*, 4970.
[8] R. Sarmiento-Perez, T. F. T. Cerqueira, S. Korbel, S. Botti, M. A. L. Marques, *Chem. Mater.* **2015**, *27*, 5957.
[9] S. Curtarolo, G. L. W. Hart, M. B. Nardelli, N. Mingo, S. Sanvito, O. Levy, *Nat. Mater.* **2013**, *12*, 191.
[10] M. S. Woodley, R. Catlow, *Nat. Mater.* **2008**, *7*, 937.
[11] R. A. Oganov, O. A. Lyakhov, M. Valle, *Acc. Chem. Res.* **2011**, *44*, 227.
[12] Y. Hinuma, T. Hatakeyama, Y. Kumagai, L. A. Burton, H. Sato, Y. Muraba, S. Iimura, H. Hiramatsu, I. Tanaka, H. Hosono, F. Oba, *Nat. Commun.* **2016**, *7*, 11962.
[13] P. Lu, D. Liang, Y. Chen, C. Zhang, R. Quhe, S. Wang, *Sci. Rep.* **2017**, *7*, 10594.
[14] I. Gherasoiu, K. M. Yu, M. Hawkridge, L. A. Reichertz, W. Walukiewicz, *Semicond. Sci. Technol.* **2019**, *34*, 025014.
[15] B. Daudin, G. Mula, P. Peyla, *Phys. Rev. B* **2000**, *61*, 10330.
[16] T. Suski, P. Perlin, A. Pietraszko, M. Leszczynski, M. Bockowski, I. Grzegory, S. Porowski, *Phys. Status Solidi A* **1999**, *176*, 343.
[17] L. R. Doolittle, *Nucl. Instrum. Methods Phys. Res., Sect. B* **1986**, *15*, 227.
[18] G. Mula, B. Daudin, C. Adelmann, P. Peyla, *MRS Internet J. Nitride Semicond. Res.* **2000**, *5*, 202.
[19] D. E. Partin, D. J. Williams, M. O'Keeffe, *J. Solid State Chem.* **1997**, *132*, 56.
[20] V. Bougrov, M. E. Levinshtein, S. L. Rumyantsev, A. Zubrilov, in *Properties of Advanced Semiconductor Materials GaN, AlN, InN, BN, SiC, SiGe* (Eds.: M. E. Levinshtein, S. L. Rumyantsev, M. S. Shur), John Wiley & Sons, Inc., New York **2001**, pp. 1–30.
[21] W. Qian, M. Skowronski, G. R. Rohrer, in *III-Nitride, SiC, and Diamond Materials for Electronic Devices* (Eds.: D. K. Gaskill, C. D. Brandt, R. J. Nemanich), Material Research Society, Pittsburgh, PA **1996**, pp. 475–486.
[22] K. Kanaya, S. Okayama, *J. Phys. D: Appl. Phys.* **1972**, *5*, 43.
[23] R. C. Murthy, *Nature* **1965**, *207*, 398.
[24] D. G. Zhao, S. J. Xu, M. H. Xie, S. Y. Tong, *Appl. Phys. Lett.* **2003**, *83*, 677.
[25] J. Chen, W. Yi, T. Kimura, S. Takashima, M. Edo, T. Sekiguchi, *Appl. Phys. Express* **2019**, *12*, 051010.
[26] Q. Yan, A. Janotti, M. Scheffler, C. G. Van de Walle, *Appl. Phys. Lett.* **2012**, *100*, 142110.
[27] Z. Xie, Y. Sui, J. Buckeridge, C. Richard, A. Catlow, T. W. Keal, P. Sherwood, A. Walsh, M.R. Farrow, D. O. Scanlon, S. M. Woodley, A. A. Sokol, *J. Phys. D: Appl. Phys.* **2019**, *52*, 335104.
[28] J. W. Huang, T. F. Kuech, H. Lu, I. Bhat, *Appl. Phys. Lett.* **1996**, *68*, 17.
[29] W. Gotz, R. S. Kern, C. H. Chen, H. Liu, D. A. Steigerwald, R. M. Fletcher, *Mater. Sci. Eng. B* **1999**, *59*, 211.
[30] K. Kumakura, T. Makimoto, N. Kobayashi, *J. Appl. Phys.* **2003**, *93*, 3370.
[31] B. N. Pantha, A. Sedhain, J. Li, J. Y. Lin, H. X. Jianga, *Appl. Phys. Lett.* **2009**, *95*, 261904.
[32] QuantumATK Manual, https://docs.quantumatk.com/manual/DFTLCAO.html (accessed: December 2019).
[33] Á. M. García, R. Valero, F. Illas, *J. Phys. Chem. C* **2017**, *121*, 18862.
[34] F. Tran, P. Blaha, *Phys. Rev. Lett.* **2009**, *102*, 226401.
[35] V. Popescu, A. Zunger, *Phys. Rev. B* **2012**, *85*, 085201.
[36] V. Popescu, A. Zunger, *Phys. Rev. Lett.* **2010**, *104*, 236403.
[37] M. W. Haverkort, I. S. Elfimov, G. A. Sawatzky, arXiv:1109.4036, **2011**.
[38] M. Grioni, Ch. R. Ast, D. Pacilé, M. Papagno, H. Berger, L. Perfetti, *New J. Phys.* **2005**, *7*, 106.
[39] T. P. Chow, M. Ghezzo, in *III-Nitride, SiC, and Diamond Materials for Electronic Devices* (Eds.: D. K. Gaskill, C. D. Brandt, R. J. Nemanich), Material Research Society, Pittsburgh, PA **1996**, pp. 69–73.
[40] J. Wu, W. Walukiewicz, K. M. Yu, J. W. Ager III, E. E. Haller, H. Lu, W. J. Schaff, *Appl. Phys. Lett.* **2002**, *80*, 4741.

 © 2020 WILEY-VCH Verlag GmbH & Co. KGaA, Weinheim